Supplementary Material

The Assembly of Grid-type Lanthanide Cluster

Jinsong Li [1], Fan Zhang [1], Xuefeng, Guo [2], Dan Liu [2,*] and Jianfeng Wu [1,*]

[1] School of Chemistry and Chemical Engineering, Northwestern Polytechnical University, Xi'an 710072, China
[2] Institute of Flexible Electronics (IFE), Northwestern Polytechnical University, Xi'an 710072, China
* Correspondence: iamdliu@nwpu.edu.cn (D.L.); jf.wu.chem@gmail.com (J.W.)

Contents:

S1. General Synthetic Considerations

All chemicals and solvents were commercially obtained and used as received without any further purification. Both 4,6-dihydrazineylpyrimidine and 6-(hydroxymethyl)-2-carbaldehyde-pyridine were synthesized by the procedure based on the literature.[1,2] The IR measurements of solid samples were performed on a Perkin–Elmer Fourier transform infrared (FTIR) spectrophotometer using the reflectance technique (4000–400 cm^{-1}), and samples were prepared as KBr disks. IR bands (Figure S7) were labeled according to their relative intensities with vs. (very strong), s (strong), m (medium), and w (weak). Elemental analyses for C, H, and N were carried out on a Perkin-Elmer 2400 analyzer. ^1H NMR spectra were recorded on a Bruker Avance 500 MHz spectrometer. Chemical shifts are reported in ppm relative to residual proton or carbon signals of the solvents DMSO-d_6 (δ_H = 2.50 ppm).

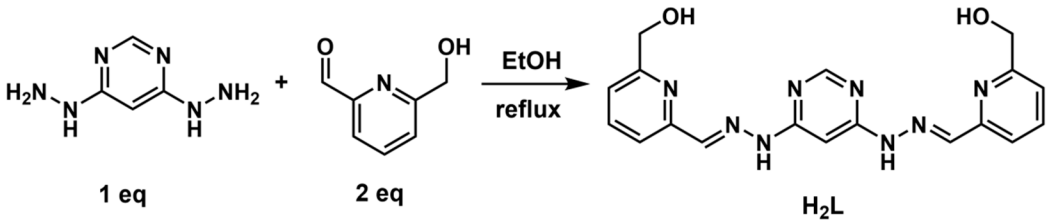

Figure S1. Schematic drawings of the synthetic route of ligand **H_2L**.

S2. NMR Spectroscopy

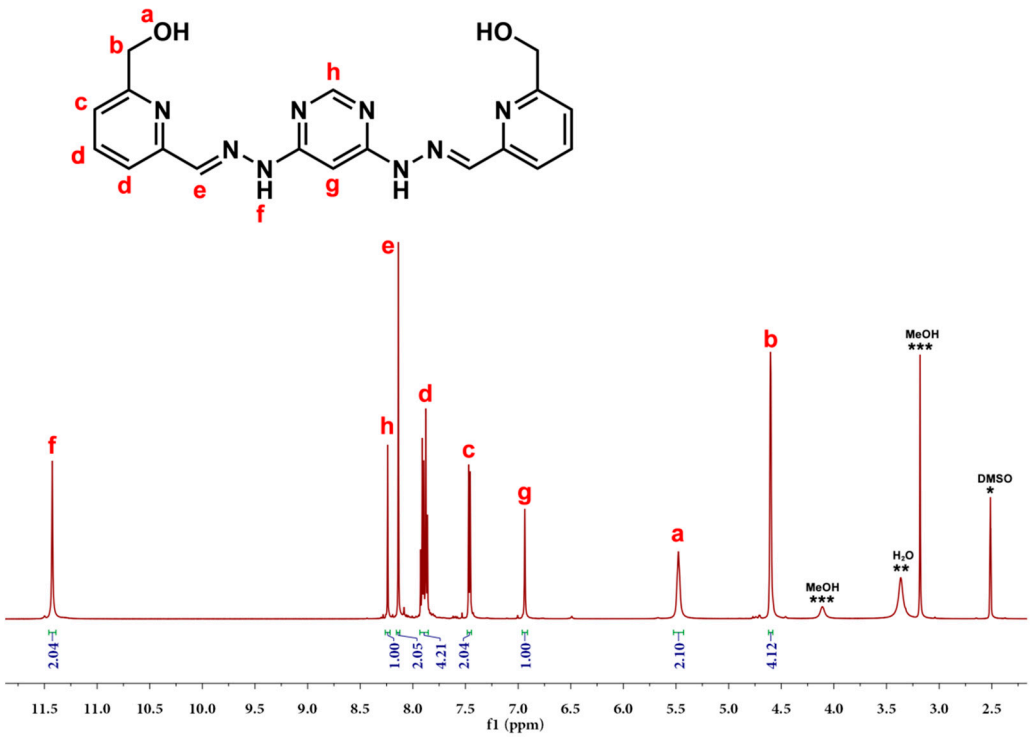

Figure S2. ^{1}H-NMR spectrum of ligand **H_2L** in DMSO-d_6 recorded at room temperature. Solvent peaks are marked with asterisks (DMSO-d_6, *; H_2O, **; MeOH, ***).

S2. IR spectra

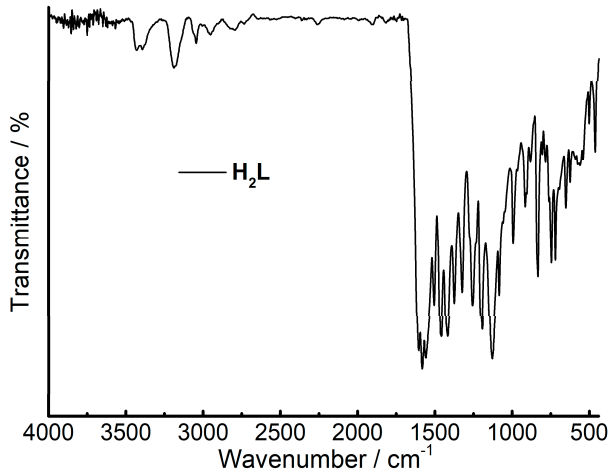

Figure S3. IR spectrum of solid samples of ligand **H_2L**.

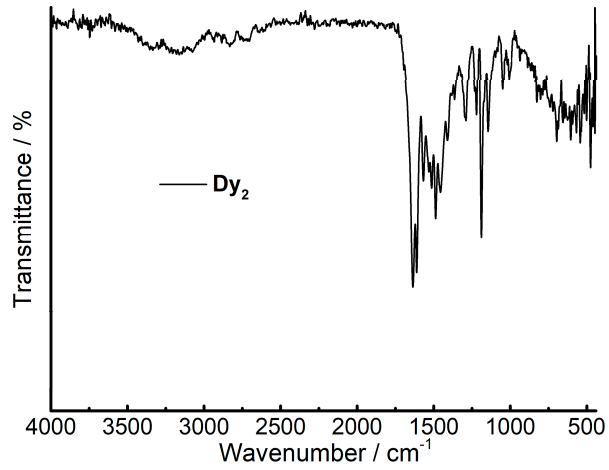

Figure S4. IR spectrum of solid samples of complex **Dy2**.

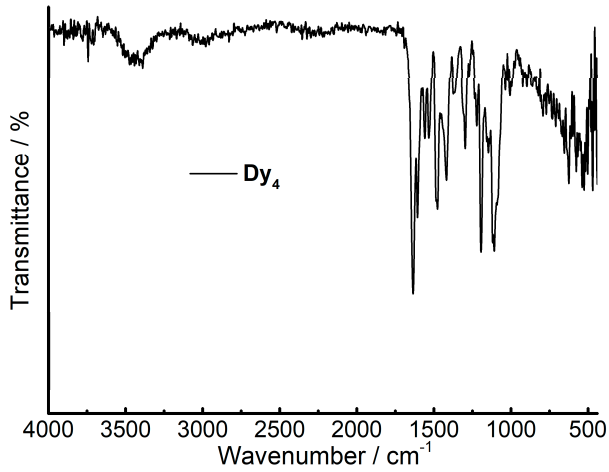

Figure S5. IR spectrum of solid samples of complex **Dy4**.

S3. Crystallographic Details

Table S1. Crystallographic data of **Dy2** and **Dy4**.

Complexes	**Dy2**	**Dy4**
empirical formula	$C_{18}H_{44}Br_6Dy_2N_8O_{15}$	$C_{84}H_{120}Cl_4Dy_4N_{32}O_{40}$
formula weight, g·mol^{-1}	1417.07	3009.91
crystal size, mm^3	0.21 × 0.19 × 0.17	0.22 × 0.21 × 0.2
crystal system	Triclinic	Tetragonal
space group	*P-1*	*P4$_2$/nmc*
T, K	293(2)	296.15
λ, Å	0.71073	0.71073
a, Å	11.5795(19)	20.7954(6)
b, Å	13.976(2)	20.7954(6)
c, Å	14.945(3)	13.6931(7)
α, °	113.935(3)	90
β, °	92.357(4)	90
γ, °	110.104(3)	90
V, Å^3	2029.5(6)	5921.6(5)
Z	2	2
ρ (cal), g·cm^{-3}	2.319	1.688
F(000)	1340.0	3000.0
2θ range [°]	3.05 to 52.152	3.562 to 52.126

*T*min / *T*max	0.152 / 0.195	0.560 / 0.585
measured refl.	12854	35701
unique refl. [*R*int]	7984, 0.0455	3103, 0.0638
goodness-of-fit (F^2)	1.015	1.085
data / restr. / param.	7984 / 8 / 471	3103 / 242 / 230
*R*1, *wR*2 ($I > 2\sigma(I)$)	0.0465, 0.1093	0.0572, 0.1629
*R*1, *wR*2 (all data)	0.0654, 0.1187	0.0871, 0.1933
res. el. dens. [e·Å^{-3}]	2.16 / −1.49	1.95 / −0.81

$R_1 = \sum(|F_0|-|F_c|) / \sum|F_0|; \quad \omega R_2 = \left[\sum\omega(|F_0|-|F_c|)^2 / \sum\omega F_0^2\right]^{1/2}$

Table S2. Selected bond distances (Å) in complexes **Dy2** and **Dy4**.

Dy2				**Dy4**	
Dy1-N4	2.512(6)	Dy2-N7	2.569(7)	Dy1-N2	2.488(6)
Dy1-N2	2.531(6)	Dy2-N8	2.498(6)	Dy1-N2#	2.488(6)
Dy1-N1	2.522(6)	Dy2-N5	2.525(6)	Dy1-N4#	2.543(6)
Dy1-O1	2.447(5)	Dy2-O2	2.388(5)	Dy1-N4	2.543(6)
Dy1-O12	2.371(5)	Dy2-O7	2.398(6)	Dy1-N1	2.437(3)
Dy1-O8	2.384(5)	Dy2-O5	2.437(6)	Dy1-N1#	2.437(6)
Dy1-O10	2.423(6)	Dy2-O4	2.447(6)	Dy1-O1	2.273(6)
Dy1-O9	2.380(6)	Dy2-O3	2.409(5)	Dy1-O1#	2.273(6)
Dy1-O11	2.462(5)	Dy2-O6	2.419(6)		

Symmetry code: # 1-Y, 1-X, 1/2-Z;

Table S3. Selected bond angles (°) in complexes **Dy2** and **Dy4**.

Dy2				**Dy4**	
N4-Dy1-N1	123.40(19)	O2-Dy2-N7	120.8(2)	N2-Dy1-N4#	82.4(2)
O1-Dy1-N2	121.94(19)	O2-Dy2-O7	75.5(2)	N4#-Dy1-N4	77.7(3)
O1-Dy1-O11	122.8(2)	O2-Dy2-O4	112.9(2)	N1-Dy1-N4#	87.81(18)
O12-Dy1-N4	82.4(2)	O7-Dy2-N8	75.1(2)	N1-Dy1-N4	126.85(18)
O12-Dy1-O10	91.9(2)	O7-Dy2-N5	77.8(2)	N1#-Dy1-N4	87.8(5)
O8-Dy1-N1	77.62(19)	O5-Dy2-N5	82.6(2)	O1-Dy1-N2#	78.1(2)
O10-Dy1-N2	131.9(2)	O4-Dy2-N7	126.3(2)	O1#-Dy1-N2#	130.3(2)
O10-Dy1-N1	89.2(2)	O3-Dy2-N7	125.7(2)	O1#-Dy1-N4	89.0(3)
O9-Dy1-N4	89.1(2)	O3-Dy2-N8	79.9(2)	O1#-Dy1-N1	88.1(2)
O9-Dy1-N1	81.5(2)	O3-Dy2-O5	104.4(2)	O1-Dy1-O1#	107.4(4)
O9-Dy1-O1	124.4(2)	O6-Dy2-N8	86.5(2)		
O11-Dy1-N2	114.6(2)	O6-Dy2-N5	80.8(2)		

Symmetry code: # 1-Y, 1-X, 1/2-Z;

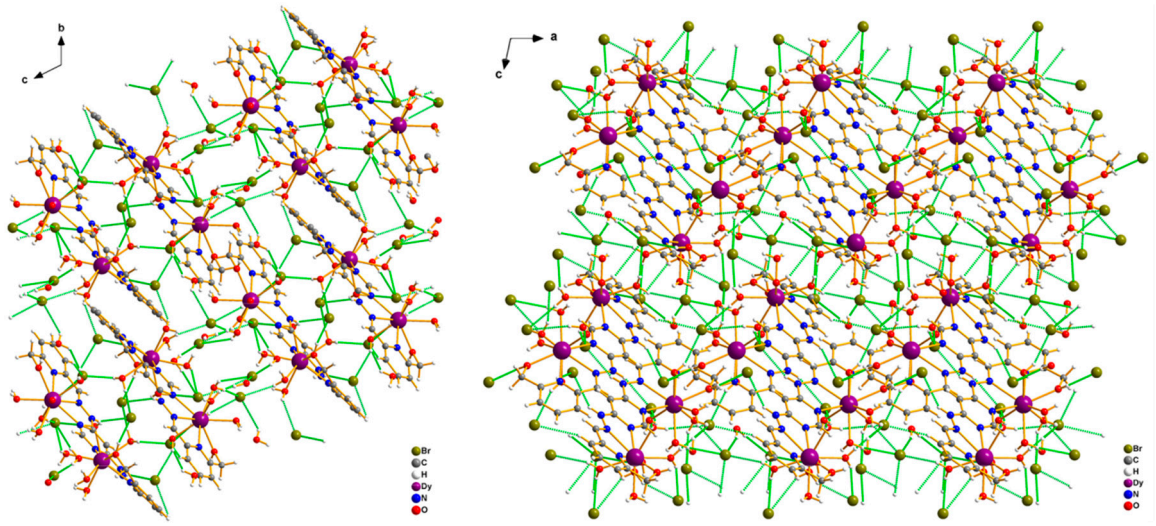

Figure S6. Packing models along *a* and *b* axes of complex **Dy2**.

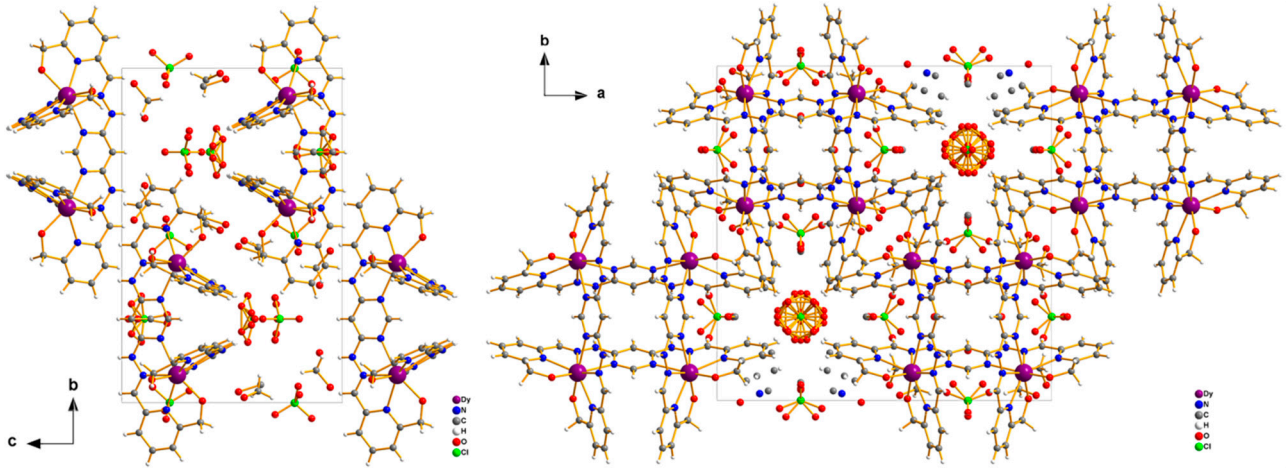

Figure S7. Packing models along *a* and *b* axes of complex **Dy4**.

Table S4. The *CShM* values calculated by *SHAPE* 2.1 [3,4] of Dy^{III} ions in **Dy2** and **Dy4**.

Dy2			**Dy4**	
Coordination Geometry	Dy1	Dy2	Coordination Geometry	Dy1
Johnson triangular cupola J3 (C3v)	14.326	15.714	Hexagonal bipyramid (D6h)	13.146
Capped cube J8 (C4v)	8.619	8.037	Cube (Oh)	11.207
Spherical-relaxed capped cube (C4v)	7.510	7.052	Square antiprism (D4d)	6.016
Capped square antiprism J10 (C4v)	2.557	1.465	Triangular dodecahedron (D2d)	3.675
Spherical capped square antiprism (C4v)	1.470	0.743	Johnson gyrobifastigium J26 (D2d)	10.056
Tricapped trigonal prism J51 (D3h)	2.443	2.962	Johnson elongated triangular bipyramid J14 (D3h)	22.625
Spherical tricapped trigonal prism (D3h)	1.508	1.865	Biaugmented trigonal prism J50 (C2v)	4.037
Tridiminished icosahedron J63 (C3v)	11.995	11.488	Biaugmented trigonal prism (C2v)	3.284
Hula-hoop (C2v)	9.342	10.518	Snub diphenoid J84 (D2d)	3.944
Muffin (Cs)	1.369	1.292		

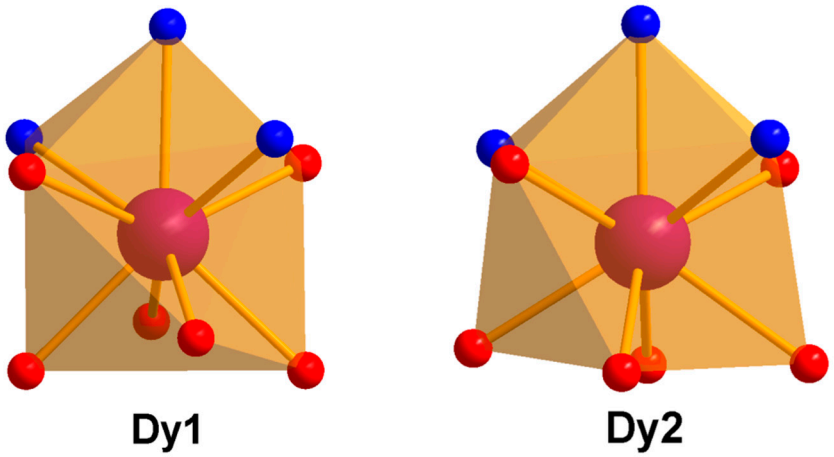

Figure S8. Coordination polyhedrons of Dy^{III} ions in complex **Dy**$_2$.

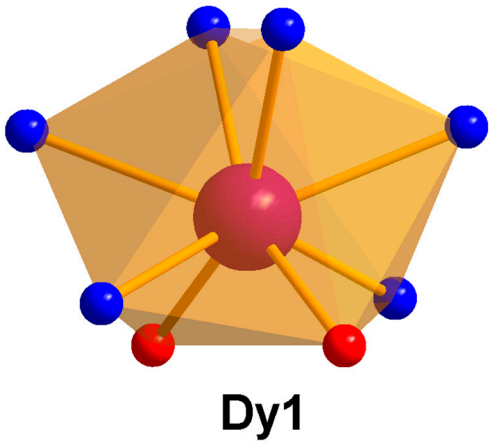

Figure S9. Coordination polyhedrons of Dy^{III} ions in complex **Dy**$_4$.

S5. Direct current (dc) magnetic susceptibility measurements

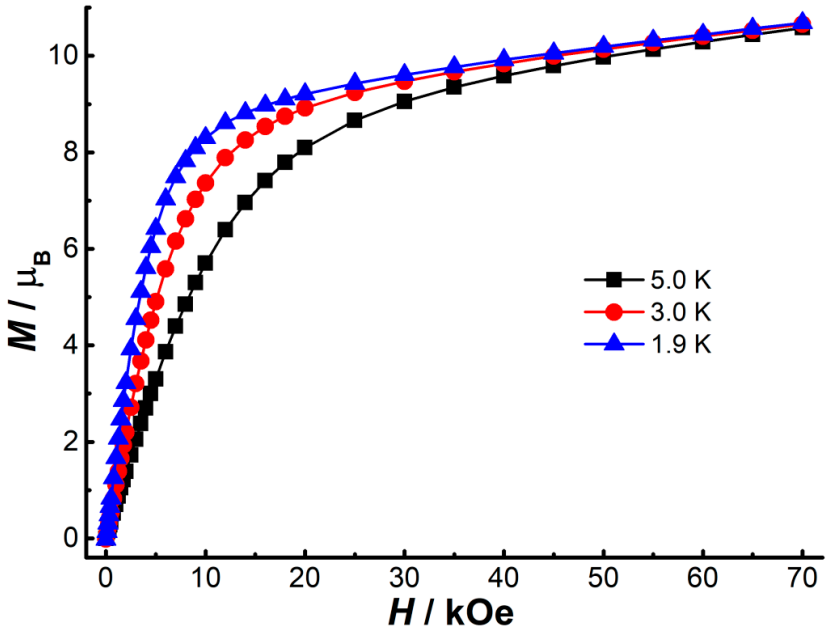

Figure S10. Molar magnetization (M) vs. field (H) of **Dy**$_2$ at indicated temperatures.

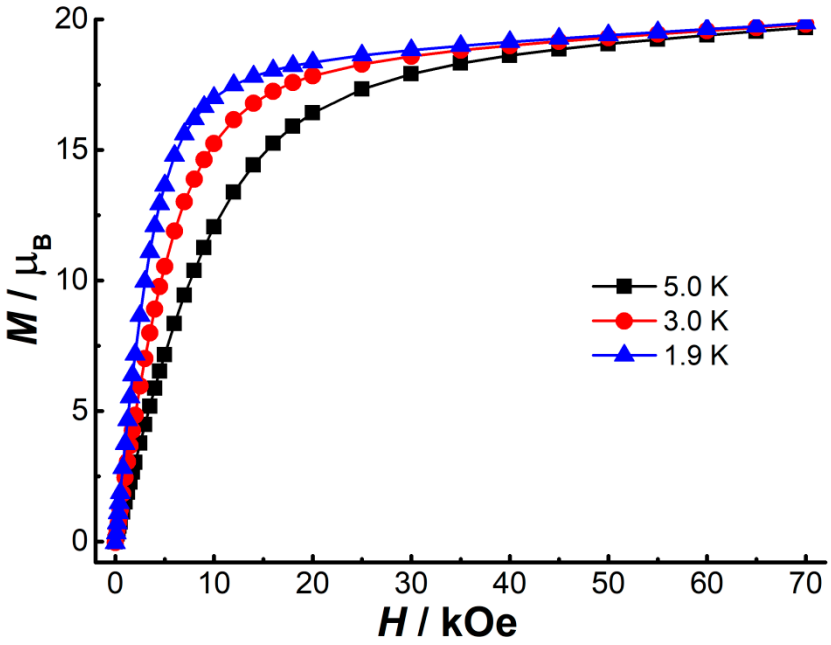

Figure S11. Molar magnetization (*M*) vs. field (*H*) of **Dy**$_4$ at indicated temperatures.

S6. Alternating current (ac) magnetic susceptibility measurements

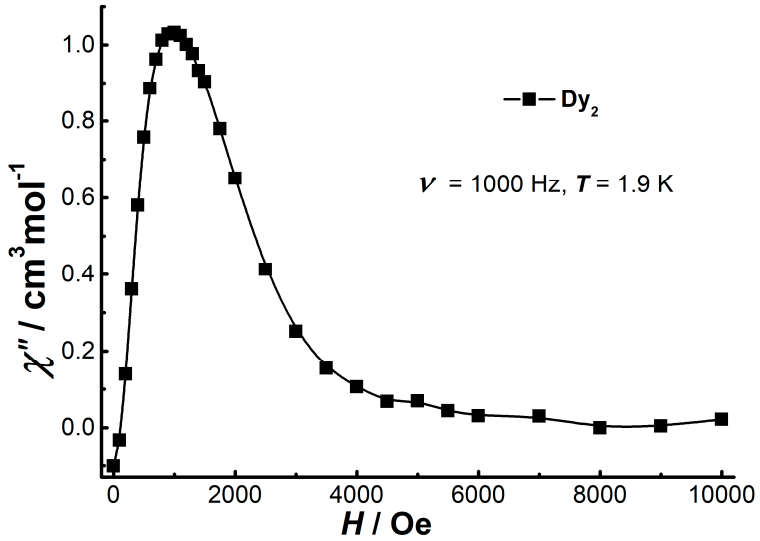

Figure S12. Field-dependent out-of-phase ac susceptibility of **Dy**$_2$ at 1.9 K with a frequency of 1000 Hz.

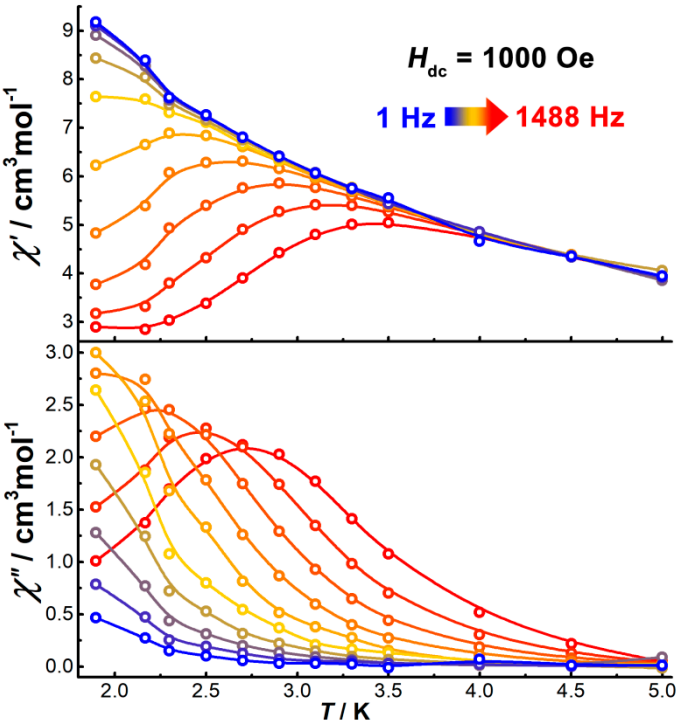

Figure S13. Temperature-dependent ac susceptibility of **Dy**$_2$ at indicated frequencies under 1000 Oe dc field.

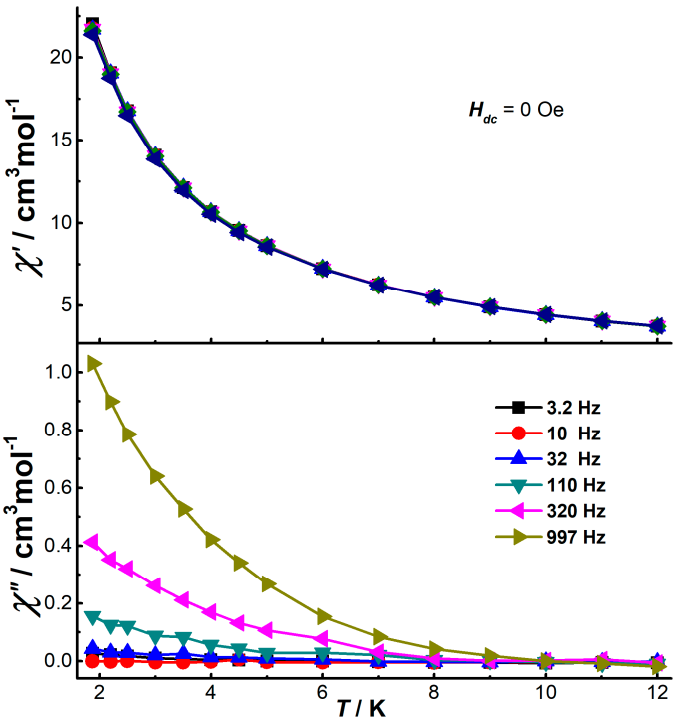

Figure S14. Temperature-dependent ac susceptibility of **Dy**$_4$ at zero dc field.

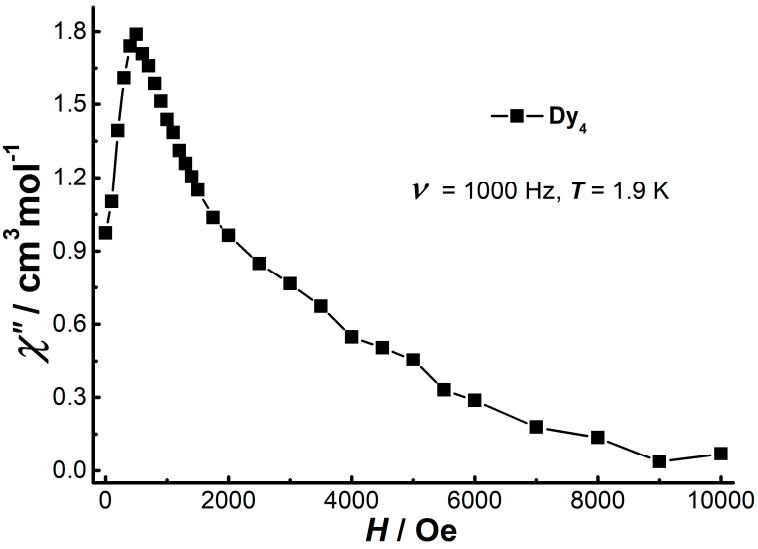

Figure S15. Field-dependent ac susceptibility of **Dy**$_4$ at 1.9 K with a frequency of 1000 Hz.

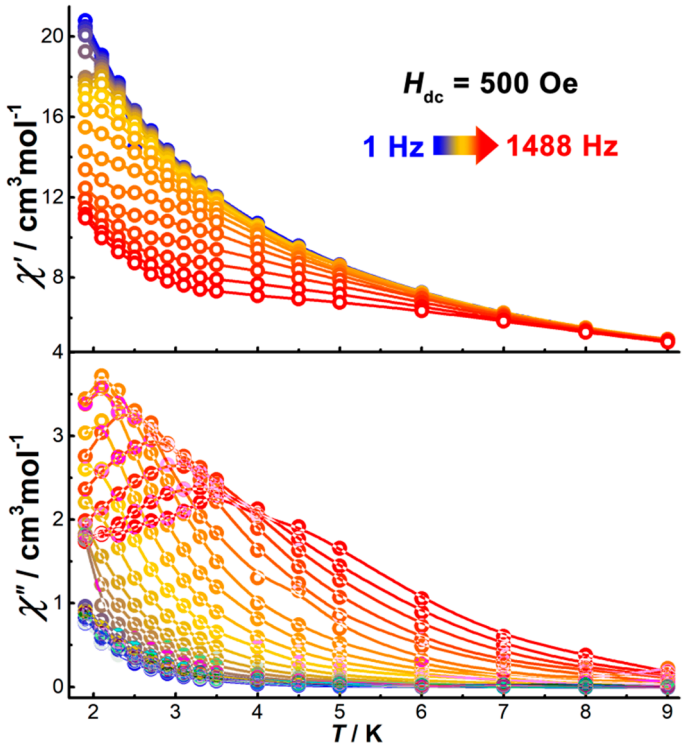

Figure S16. Temperature-dependent ac susceptibility of **Dy**$_4$ at indicated frequencies under 500 Oe dc field.

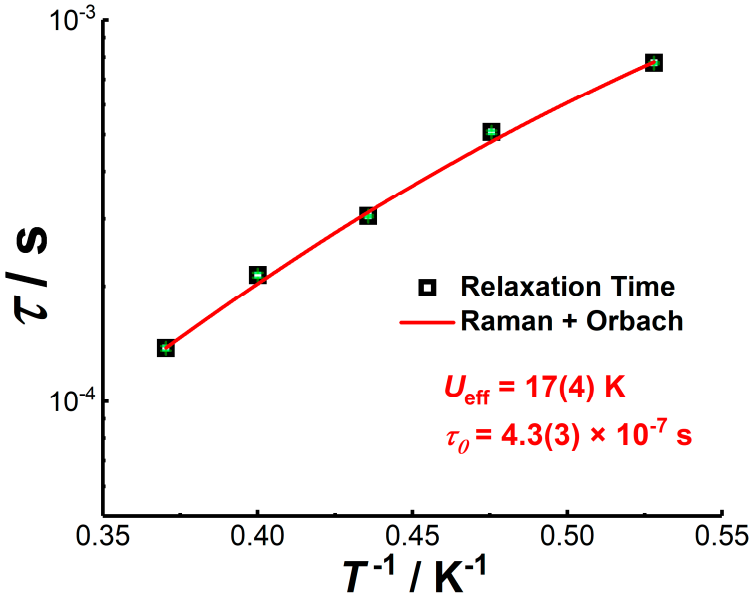

Figure S17. Plots of τ vs. T^{-1} for **Dy**$_2$ obtained under 1000 Oe dc fields. The red lines represent the best fit.

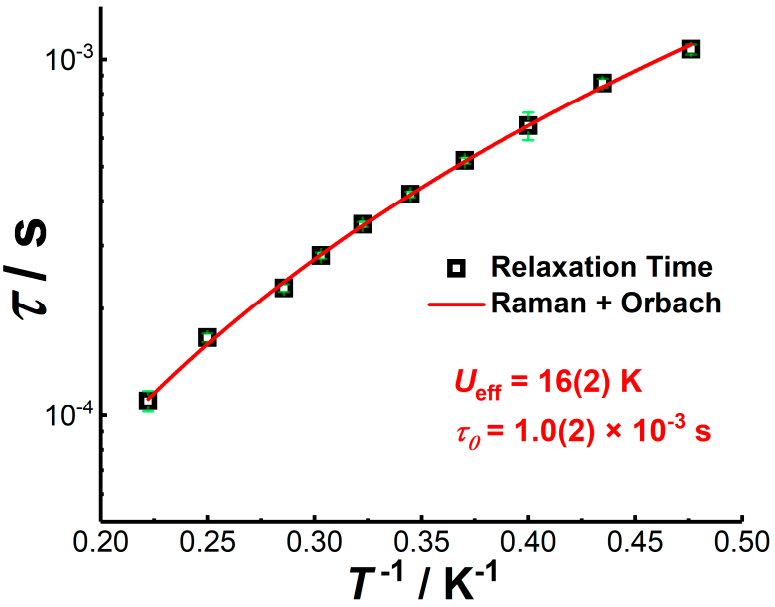

Figure S18. Plots of τ vs. T^{-1} for **Dy**$_4$ obtained under 500 Oe dc fields. The red lines represent the best fit.

S7. CC-Fit results

Table S5. CC-Fit results for frequency-dependent ac susceptibility of **Dy**$_2$ under 1000 Oe dc field.

T / K	χ_S	χ_T	τ / s	τ_err	α	α_err
1.89385	2.74234	9.55077	7.72543E-4	5.12499E-6	0.05495	0.00392
2.10264	2.48729	8.70245	5.07341E-4	5.11869E-6	0.0582	0.00578
2.29491	2.34242	7.89523	3.04647E-4	2.0003E-6	0.05425	0.0035
2.49951	2.16375	7.52685	2.13948E-4	3.07678E-6	0.0714	0.00657
2.69979	2.0055	7.04531	1.37468E-4	1.92458E-6	0.07621	0.00509

Table S6. CC-Fit results of frequency-dependent ac susceptibility of **Dy**$_4$ under 500 Oe dc field.

T / K	χ_S	χ_T	τ / s	τ_err	α	α_err
2.09997	0.04121	0.08594	0.00107	3.464E-5	0.20558	0.01471
2.29992	0.038	0.07985	8.57297E-4	2.42292E-5	0.18494	0.01308
2.50004	0.03533	0.07315	6.50848E-4	5.79072E-5	0.15318	0.04271
2.69997	0.03206	0.06921	5.19327E-4	1.00097E-5	0.17417	0.0085
2.89986	0.02964	0.06487	4.17852E-4	7.67784E-6	0.18093	0.00759
3.09965	0.02787	0.06105	3.43886E-4	5.66543E-6	0.17821	0.0065
3.29977	0.0258	0.05762	2.80857E-4	5.53424E-6	0.18457	0.00715
3.49982	0.02395	0.05462	2.28093E-4	5.53726E-6	0.19263	0.00795
4.00014	0.02219	0.04826	1.65342E-4	4.64493E-6	0.19196	0.00798
4.50009	0.0192	0.04325	1.09882E-4	7.36767E-6	0.21809	0.01437

Table S7. Parameters with standard error obtained from fitting the plots of the relaxation time τ vs. $1/T$ for **Dy**$_2$ and **Dy**$_4$.

T / K	U_{eff} / K	τ_0 / s	C	n
Dy$_2$ (1000 Oe)	17(4)	4.2(3)E-7	144(5)	3(0.3)
Dy$_4$ (500 Oe)	16(2)	1.0(2)E-3	98(9)	3(0.8)

S8. Magellan calculations

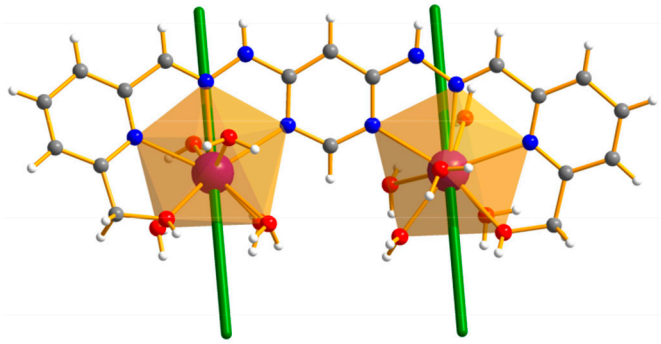

Figure S19. Top view of the orientations of the main magnetic axes of the ground state of **Dy**$_2$.

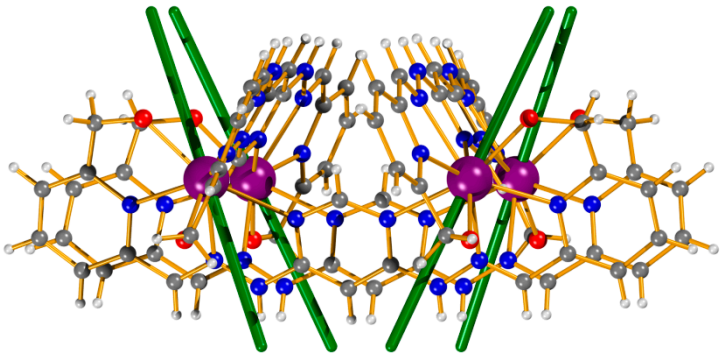

Figure S20. Side view of the orientations of the main magnetic axes of the ground state of **Dy**$_4$.

S9. References

1. Uppadine, L.H.; Gisselbrecht, J.-P.; Kyritsakas, N.; Nättinen, K.; Rissanen, K.; Lehn, J.-M. Mixed-Valence, Mixed-Spin-State, and Heterometallic [2×2] Grid-type Arrays Based on Heteroditopic Hydrazone Ligands: Synthesis and Electrochemical Features. *Chem. Eur. J.* **2005**, *11*, 2549-2565, doi:10.1002/chem.200401224.
2. Join, B.; Möller, K.; Ziebart, C.; Schröder, K.; Gördes, D.; Thurow, K.; Spannenberg, A.; Junge, K.; Beller, M. Selective Iron-Catalyzed Oxidation of Benzylic and Allylic Alcohols. **2011**, *353*, 3023-3030, doi:https:1002/adsc.201100210.
3. Casanova, D.; Alemany, P.; Bofill, J.M.; Alvarez, S. Shape and Symmetry of Heptacoordinate Transition-Metal Complexes: Structural Trends. *Chem. Eur. J.* **2003**, *9*, 1281-1295, doi:10.1002/chem.200390145.
4. Alvarez, S.; Llunell, M. Continuous symmetry measures of penta-coordinate molecules: Berry and non-Berry distortions of the trigonal bipyramid. *J. Chem. Soc. Dalton Trans.* **2000**, 10.1039/B004878J, 3288-3303, doi:10.1039/B004878J.